Investigating the transport mechanisms governing the oxidation of Hastelloy BC-1 by *in situ* ToF-SIMS

Jeffrey D. Henderson[a], Antoine Seyeux[b], Sandrine Zanna[b], Mark C. Biesinger[c],
David W. Shoesmith[a,c], James J. Noël[a,c,*], Philippe Marcus[b,**]

[a] *Department of Chemistry, Western University, London, ON, N6A 5B7, Canada*
[b] *Chimie ParisTech, CNRS, PSL Research University, IRCP-PCS, 75005, Paris, France*
[c] *Surface Science Western, Western University, London, ON, N6G 0J3, Canada*

ARTICLE INFO

ABSTRACT

This paper presents insight into the structure and transport mechanisms involved in the surface oxidation of Hastelloy BC-1, gained by means of *in situ* time-of-flight secondary ion mass spectrometry and X-ray photoelectron spectroscopy. The native, air-formed oxide, comprising Cr-rich (inner) and Mo-rich (outer) layers, was found to be on the order of 1–2 nm thick. Oxide thickness did not change when the temperature was increased to 300 °C in oxygen atmosphere but increased to ~10 nm after exposure at 500 °C. The mechanisms of oxide growth/ maintenance as well as observations on the effect of elevated temperatures on oxide structure are discussed.

1. Introduction

A major component of corrosion research focuses on how individual alloying elements influence the properties of an alloy. Chromium additions have been shown to lead to the formation of a Cr-rich oxide, responsible for passive behavior [1–5]. Additions of molybdenum to Cr-containing alloys are known to stabilize the barrier oxide in acidic media, such as HCl, as well as increase resistance to localized corrosion [1,2,5–7]. Together, the combination of Cr and Mo in both Fe- and Ni-based alloys has been characterized by a duplex (or bilayer) oxide structure, with Cr and Mo dominating the inner and outer oxides, respectively [5,8–10]. Due to their industrial relevance, including the petrochemical and chemical processing, nuclear, and aerospace industries, the nature of Cr/Mo-containing oxides remains the focus of ongoing research [11–13].

A subset of these studies has focused on gas phase, particularly low-pressure, oxidation [14–16]. Exposure of Cr-containing alloys to high temperatures is known to lead to the volatilization of the protective oxide [17,18]. This is a particularly important process in the consideration of materials for use in combustion engines and their related components (*e.g.* exhaust system) as well as supercritical water applications. Such processes necessitate a thorough understanding of surface

oxidation mechanisms. Poulain et al. investigated the kinetics of oxide growth and identified the transport of ions through oxides formed on a pure Cr substrate [19]. In their discussion of a kinetic model, the authors suggest the existence of Cr volatilization occurring at temperatures as low as 300 °C. In a separate study by Yu et al., crystallographic information pertaining to the early oxidation of Ni-Cr and Ni-Cr-Mo alloys was reported using *in situ* environmental transmission electron microscopy [20]. Although focused on higher temperatures, their results show the progression of oxide nucleation and demonstrate the benefit of alloyed-Mo in preventing the formation of voids.

Since transport processes in oxides are governed by the oxide defect structure, in addition to considering the mechanisms occurring for oxides grown under controlled environments it is important also to consider the oxidation mechanisms occurring for oxides initially formed in air, *i.e.,* native oxides. While working with a native oxide limits the kinetic information pertaining to early oxide formation, the effects of applied temperature on oxide structure, as well as transport processes, can still be studied. Herein, the native oxide existing on Hastelloy BC-1 is investigated by a combination of *in situ* time-of-flight secondary ion mass spectrometry (ToF-SIMS) and X-ray photoelectron spectroscopy (XPS) measurements. Heating to 300 °C is demonstrated to result in minor structural changes in the oxide, although the details remain

---

unclear. At 500 °C the oxide was found to thicken due to the growth of the inner Cr-rich oxide. While oxide structure is discussed, the focus of the present work is on the transport mechanisms occurring during surface oxidation. Controlled oxidation of pre-oxidized (native oxide) Ni-Cr-Mo alloys with $^{18}O_2$ (300 and 500 °C) as an isotopic label highlights the location of O^{2-} incorporation in the oxide, allowing the transport of ions through the oxide to be determined.

2. Experimental

Samples, provided by Haynes International (Kokomo, IN, USA), were machined to dimensions of 1 cm × 1 cm × 0.3 cm. All samples were ground using wet SiC paper (P600-P2400) and polished with 6-, 3-, and 1-μm diamond suspensions. Prepared samples were ultrasonically cleaned in acetone, ethanol, and deionized water, and dried in a stream of compressed air. Following surface preparation and cleaning, samples were stored overnight in a desiccator prior to analysis.

XPS measurements were carried out on a Thermo Electron Escalab 250 spectrometer, employing a monochromatic Al Kα X-ray source (hν = 1486.6 eV). For all measurements, the pressure inside the analysis chamber was maintained at, or below, 10^{-7} Pa. Instrument calibration was performed using the $4f_{7/2}$ signal (83.95 eV) of a standard Au sample. A circular spot (diameter of 500 μm) was used to excite photoelectrons with a take-off angle of 90°. Survey spectra were recorded using a 100 eV pass energy at a step size of 1 eV. High-resolution spectra of the C 1s, O 1s, Ni 2p, Cr 2p, and Mo 3d core levels were collected using a 20 eV pass energy at a step size of 0.1 eV. Spectra were charge-corrected with reference to the aliphatic (C–C) carbon contamination signal (284.8 eV). Signal deconvolution was performed with CasaXPS software (v2.3.14) using a Shirley background subtraction. The model used to calculate an approximate film thickness from photoelectron intensities was adapted from a previously employed methodology [21,22]. A summary of the model is included in the SI. Values of inelastic mean free path (λ_X^Y) used were calculated by the TPP2M formula [23].

ToF-SIMS measurements were carried out on a dual-beam ToF-SIMS V spectrometer (ION-TOF GmbH, Muenster, Germany). Depth profiles were obtained using a dual-beam mode in which a Bi^+ ion beam was used to produce secondary ions, and a Cs^+ ion beam was used to sputter (or remove) material. Material was removed from a 500 μm × 500 μm area, while secondary ions were released from the center of the resulting crater with an area of 100 μm × 100 μm. The Bi^+ ion beam was operated at a current of 0.1 or 1.2 pA, indicated with the respective data. The latter provided sufficient ion counts to analyze trace species existing in the oxide, while the former avoided issues of detector saturation by concentrated species. For a Cs^+ beam current of 20 nA, the sputter rate was determined by surface profilometry on a sputter crater to be 0.02 nm s^{-1}. Since the resulting sputtered area was consistently deeper than the oxide film was thick, the experimentally determined sputter rate was influenced by sputtering rate of both the oxide and metallic specimen. During analyses, the pressure in the analysis chamber was maintained at < 5 × 10^{-7} Pa. At each condition (*i.e.,* temperature or oxidation time) depth profiles were collected at both 0.1 and 1.2 pA primary beam currents.

Immediately after the specimen was introduced, and prior to the application of heat, the air-formed oxide was analyzed at both primary beam currents. Due to the destructive nature of sputtering, each depth profile was collected at a different, unperturbed area on the coupon surface. The specimen was then heated to a temperature of 300 ± 1 °C using the heating stage. Modifications to the air-formed oxide due to heating were analyzed. A precision leak valve was then used to introduce a constant supply of $^{18}O_2$ into the analysis chamber, such that the partial pressure P_{18-O2} was constant at 1 × 10^{-3} Pa. After the designated oxidation time had elapsed, the leak valve was closed while the sample temperature was maintained at 300 ± 1 °C, and the chamber immediately pumped down to the base pressure

(< 5 × 10^{-7} Pa), and depth profiles were collected at the two primary beam currents. This process -oxidation and depth analysis- was carried out for 1, 5, 15, 30, and 60-min oxidation times. Following oxidations at 300 °C, the temperature was elevated to, and maintained at, 500 ± 1 °C where the coupons were again oxidized by exposure to $^{18}O_2$.

3. Results and discussion

3.1. Air-formed oxide

Ions selected for the interpretation of depth profiles include NiO_2^-, CrO_2^-, MoO_3^-, and Ni_2^-. While NiO_2^-, CrO_2^-, and MoO_3^-, are indicative of their respective oxides [15,24], Ni_2^- is associated with the underlying metal substrate [15,19]. Briefly, as the oxidized metal signals (MO_n^-) decreased into the sample, the Ni_2^- signal increased, reaching a quasi-plateau once the metallic interface was reached. Therefore, the oxide/metallic interface, and thus the oxide thickness could be interpreted relative to the location of maximum intensity or the quasi-plateau of the Ni_2^- signal [15]. To quantify thickness, depth profiles were converted from a time base to a function of depth using the experimentally determined sputter rate, 0.02 nm s^{-1}. The original sputter time and the corresponding depth are included for all depth profiles, on the upper and lower horizontal axes, respectively.

A depth profile of the initial air-formed oxide is presented in Fig. 1. The oxide was found to include an unambiguous bilayer structure. Three distinct regions were identified in Fig. 1: (i) A Mo-rich outer oxide layer, (ii) a Cr-rich inner oxide layer, and (iii) the underlying metallic substrate. Signals corresponding to MoO_3^- and CrO_2^- achieved maximum intensities at ~18 s (~0.36 nm) and ~46 s (~0.92 nm), respectively. The formation of bilayer oxides on Cr/Mo containing alloys has been extensively documented [8–10,25,26]. Recently, the origin of this bilayer structure has been attributed to the rapid diffusion of Mo through an initially formed Cr_2O_3-rich layer [11,12]. While the inner Cr-rich oxide layer is generally accepted as the barrier layer responsible for corrosion resistance [1,2], the role of the Mo has been a topic of continued investigation.

Signals for NiO_2^-, although low in intensity, overlapped with the signals for MoO_3^- and CrO_2^-, suggesting the presence of a small amount of oxidized Ni within the Cr- and Mo-rich layers. Corresponding NiO_2^- and CrO_2^- signals have been suggested to imply the possible
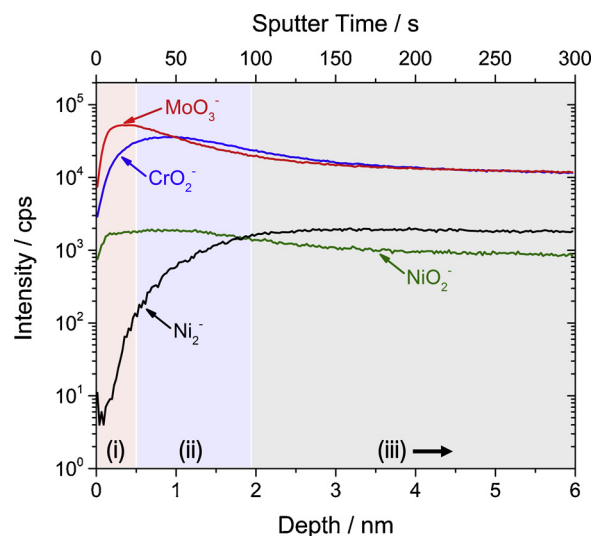
Fig. 1. ToF SIMS depth profile of the air-formed oxide present on BC-1 following the surface preparation procedure. Approximate locations of the (i) Mo- and (ii) Cr-rich layers, as well as the (iii) metallic substrate are indicated. Primary Bi^+ beam operated at 1.2 pA.
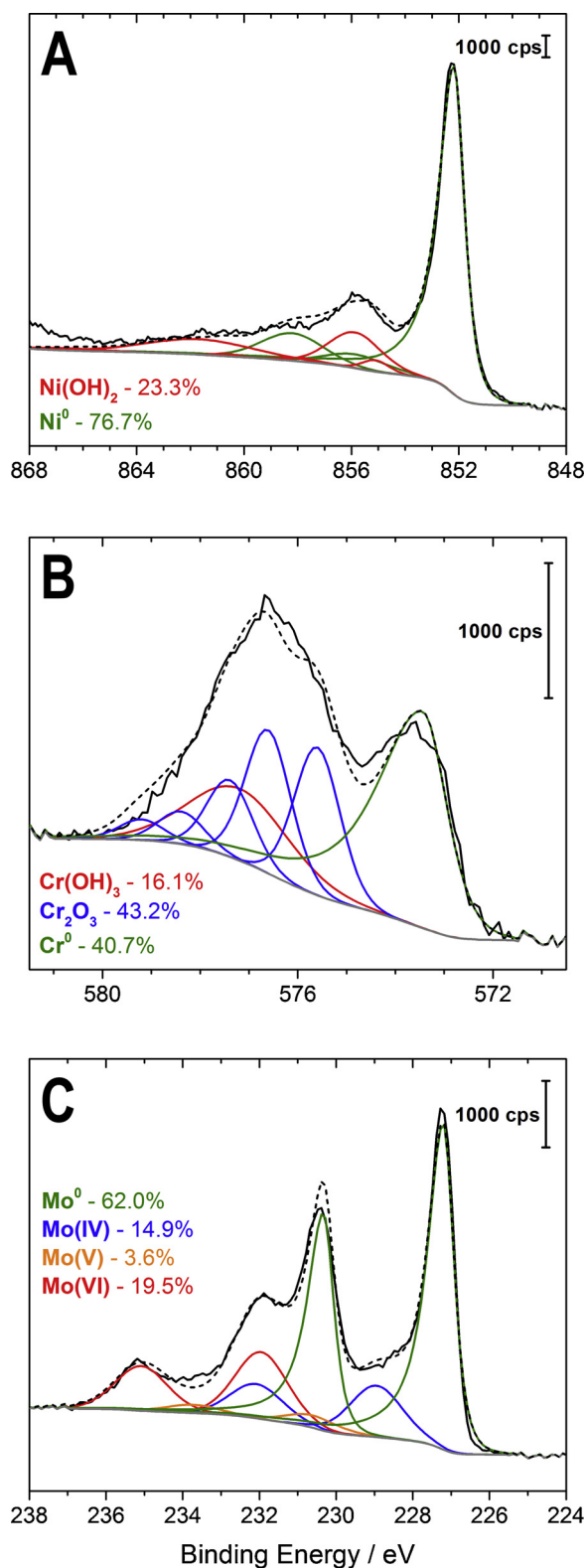
Fig. 2. High-resolution XPS spectra showing (A) Ni 2p$_{3/2}$, (B) Cr 2p$_{3/2}$, and (C) Mo 3d bands. Dashed line indicates the fit of the corresponding deconvolution.

existence of a spinel oxide, NiCr$_2$O$_4$. Spinel (or mixed) oxides have been observed following gas-phase oxidation under a range of conditions [14–16,20,27], although our XPS data were more indicative of the formation of Ni(OH)$_2$ (see below). Additionally, electrochemically grown films have also demonstrated a similar co-existence of Ni and Cr species in the inner oxide film [8,9,28,29].

Table 1

Nominal composition (%$_{wt.}$) of Hastelloy BC-1 as reported by Haynes International: ^{M} indicates maximum concentrations.

Ni	Cr	Mo	Fe	Co	Mn	Al	Si	C
Bal.	15	22	2^M	1^M	0.25	0.5^M	0.08^M	0.01^M

The air-formed oxide, present after the surface preparation procedure, was also investigated by XPS. Review of survey spectra, not shown, identified the dominant photoelectron signals to be the Ni 2p, Cr 2p, Mo 3d, O 1s, and C 1s peaks. High-resolution Ni 2p$_{3/2}$, Cr 2p$_{3/2}$, and Mo 3d spectra are presented in Fig. 2A–C along with the fit obtained by deconvolution of Ni 2p$_{3/2}$, Cr 2p$_{3/2}$, and Mo 3d$_{5/2}$ and 3d$_{3/2}$ core levels. Fitting parameters were taken from the previously published work of Biesinger et al. (Ni [30,31] and Cr [31,32]), Spevack et al. (Mo [33]), and Marcus et al. (Mo [34,35]). Taking into account the intensity ratio between the satellite and main Ni(II) peaks, it was possible to distinguish Ni(OH)$_2$ species (ratio around 0.3) [30,36,37] from spinel oxides, NiCr$_2$O$_4$ (ratio around 0.7) [31,32,38,39]. For specimens analyzed here, the experimental ratio was 0.35, suggesting that Ni(II) existed mainly as Ni(OH)$_2$.

Considering only the signals arising from the major alloying elements, Ni, Cr, and Mo, the surface concentrations (%$_{at.}$) in the oxide layer and underlying metallic substrate were determined and are summarized in Table 2. This assumes that a continuous and homogeneous oxide layer covered the underlying metallic substrate. Included in Table 2 is the nominal composition of BC-1 converted from %$_{wt.}$ (Table 1) to %$_{at.}$ for reference. Comparing the composition of underlying metal to the normalized nominal composition (converted to %$_{at.}$ from Table 1) showed that the metallic substrate existing directly below the oxide layer was depleted of Cr and Ni while enriched in Mo metal. Using the deconvolution obtained from the high-resolution spectra, the concentrations (%$_{at.}$) of the oxidized species present in the oxide film were further considered. Both the composition of the underlying metallic layer and the overlaying oxide layer are represented in Fig. 3.

A complement to ToF-SIMS (above), XPS has previously been used to demonstrate the enrichment of Mo in the outer oxide. By employing angle-resolved XPS (AR-XPS) methods, Zhang et al. demonstrated the enrichment of oxidized Mo species, including Mo(IV), Mo(V), and Mo(VI), in the outer region of the oxide [8,9]. Additionally, Mo-enrichment in the outer portion of the oxides has been observed in different Mo-containing alloys [11,21].

Considering the bilayer structure, an XPS model was developed, based on previous work [21,22,40], to approximate the total oxide thickness, as well as the thickness of the inner and outer layers, *i.e.*, the Cr- and Mo-rich oxide layers, respectively. To deal with the complexity of the apparent oxide film, several approximations were made. First, the mean free path (λ) and values of density used to characterize each layer were representative of only the major component, *i.e.*, the inner layer being Cr$_2$O$_3$ and the outer layer MoO$_3$. Second, although high-resolution XPS spectra showed that hydrated oxides comprised a portion of the air-formed oxide, for simplicity we did not distinguish hydrated oxides from their dehydrated counterparts. Thickness values are summarized in Table 2. With a total thickness of approximately 1.1 nm, the oxide was found to contain inner and outer layers of approximately the same thickness. For comparison, the oxide thickness as interpreted by

Table 2

Surface concentrations in the oxide layer and underlying metallic substrate as determined by XPS as well as the nominal composition converted to %$_{at.}$

	Ni/%$_{at.}$	Cr/%$_{at.}$	Mo/%$_{at.}$
Oxide Layer	24.6	28.3	47.2
Underlying Metallic Substrate	60.3	10.2	29.5
Nominal Composition	67.1	18.3	14.6
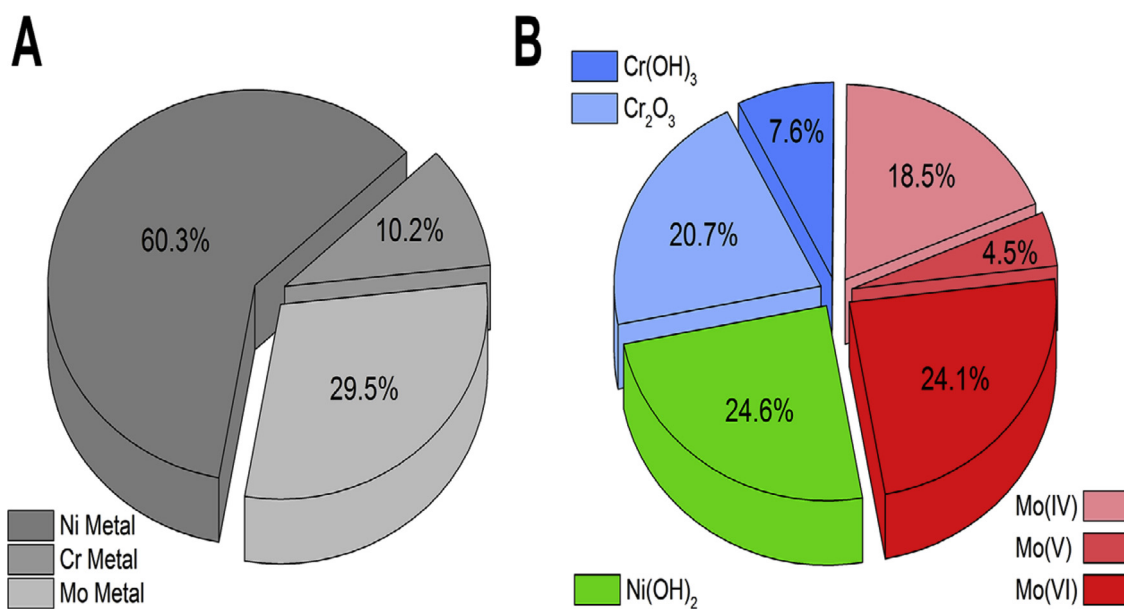
Fig. 3. Normalized surface composition ($\%_{at.}$) of (A) Ni, Cr, and Mo in the underlying metallic layer and of (B) the oxidized species present in the overlaying oxide layer.

ToF-SIMS (Fig. 1), *i.e.,* the location of the Ni_2^- plateau intensity, suggested that the air-formed oxide was approximately 2 nm thick. In the literature, oxides present on Ni- and Fe-based alloys are typically on the order of a few nm [10,13,21,41,42], indicating that the thickness measurements here were reasonable. Differences in thickness measured by XPS and ToF-SIMS likely resulted from differences in the assumptions and approximations made in interpreting the data from the two measurements. While the XPS model included various approximations, as discussed above, thickness measurements using ToF-SIMS data were determined based on the assumption that the sputtering rate of the oxide was the same as that of the metallic substrate. Nonetheless, the results were in fairly good agreement (1–2 nm).

3.2. Intermediate temperature oxidation

Following sample heating to 300 °C, depth profiles were taken at various stages of oxidation. Shown in Fig. 4A-D are the profiles acquired after 0, 1, 15, and 60-min oxidation periods, respectively.

Comparison of the oxide depth profile after the application of heat (Fig. 4A) to that of the original air-formed oxide (Fig. 1) revealed the effect of elevated temperature (300 °C) on the structure of the oxide. While no major changes in oxide thickness were observed following heating to 300 °C, the bilayer was found to undergo structural modification: specifically, the depth at which the maximum intensity of MoO_3^- was found decreased, suggesting slight thinning of the Mo-rich layer. Additionally, the development of a shoulder in the MoO_3^- signal was observed; the location is indicated by an asterisk (*) in Fig. 4A. While most of the Mo oxide appeared to have remained in the outermost region of the film, the location of the Mo oxide shoulder, within the Cr-rich layer, suggested oxide mobility resulting from the application of heat. While processes of diffusion and/or migration were an obvious explanation, the volatility of oxides at intermediate/high temperatures may also have played a role [18,19,43]. The exact reason for this structural modification is, at this point, unclear and will be the focus of future work. Although increased temperatures caused this structural modification, exposure to O_2 was found to reverse this modification, as discussed later.

The *in situ* re-oxidation of the native oxide (at 300 °C) with isotopic $^{18}O_2$ gas, might be expected to result in the thickening of the oxide film, though this was not observed. Instead, the oxide film was found to

remain at a thickness of approximately 2 nm, even after the longest exposure to $^{18}O_2$. In a previous study, controlled oxidation of Ni-Cr-Fe alloys resulted in comparable steady-state oxide thicknesses, approximately 2.5 nm after only 1 -h of exposure to O_2 (1.2×10^{-4} Pa) at 300 °C [15]. However, in the previous study, the initial surface was free from air-formed oxide, allowing the kinetics of early oxidation to be observed. In this study, the presence of a pre-existing oxide made the extraction of oxidation kinetics problematic. According to the Mott-Cabrera model, once an oxide has reached a limiting thickness, recrystallization is required for further growth to proceed [44,45]. Despite the elevated temperature, this process requires enough time for nucleation of crystalline oxide to occur.

While the oxide film thickness did not change after exposure to $^{18}O_2$, the pronounced bilayer structure was found to return. As previously mentioned, the application of heat (300 °C) resulted in a decreased intensity of the MoO_3^- signal from the outer oxide and the appearance of a shoulder within the Cr-rich layer. Inspection of Fig. 4B-D revealed the gradual loss of the MoO_3^- shoulder and the re-establishment of a well-defined bilayer structure. After a total oxidation time of 15 min, Fig. 4C, the intensity of the MoO_3^- signal from the outer oxide was found to increase and the shoulder disappear. The re-establishment of the Mo-rich outer layer continued with time. At the longest exposure, Fig. 4D, the MoO_3^- signal originated mainly from the outer region of the oxide, as it did in the initial air-formed oxide.

In contrast to measurements made at 300 °C, a measurement made at 500 °C showed the thickening of the oxide film. The depth profile determined following an oxidation period of 5 min at 500 °C is shown in Fig. 5A. Here, an increase in temperature was again found to result in a decreased intensity of the MoO_3^- (and $Mo^{18}O_3^-$) signal(s) in the outer portion of the oxide and a shoulder extending throughout the rest of the oxide layer. Increases in the total film thickness appeared to be the result of the growth of the inner Cr-rich layer.

The approximate film thicknesses determined by ToF-SIMS depth profiles at the various experimental conditions discussed above are summarized in Fig. 5B. Approximate depth of transitions between metal/oxide and between the Cr-rich and Mo-rich regions of the oxide were determined by the location of 80% intensity of the Ni_2^- signal and the location between maximum intensities of CrO_2^- and MoO_3^- signals, respectively. Whether signals incorporating ^{16}O or ^{18}O were used for this measurement depended on their relative intensities.
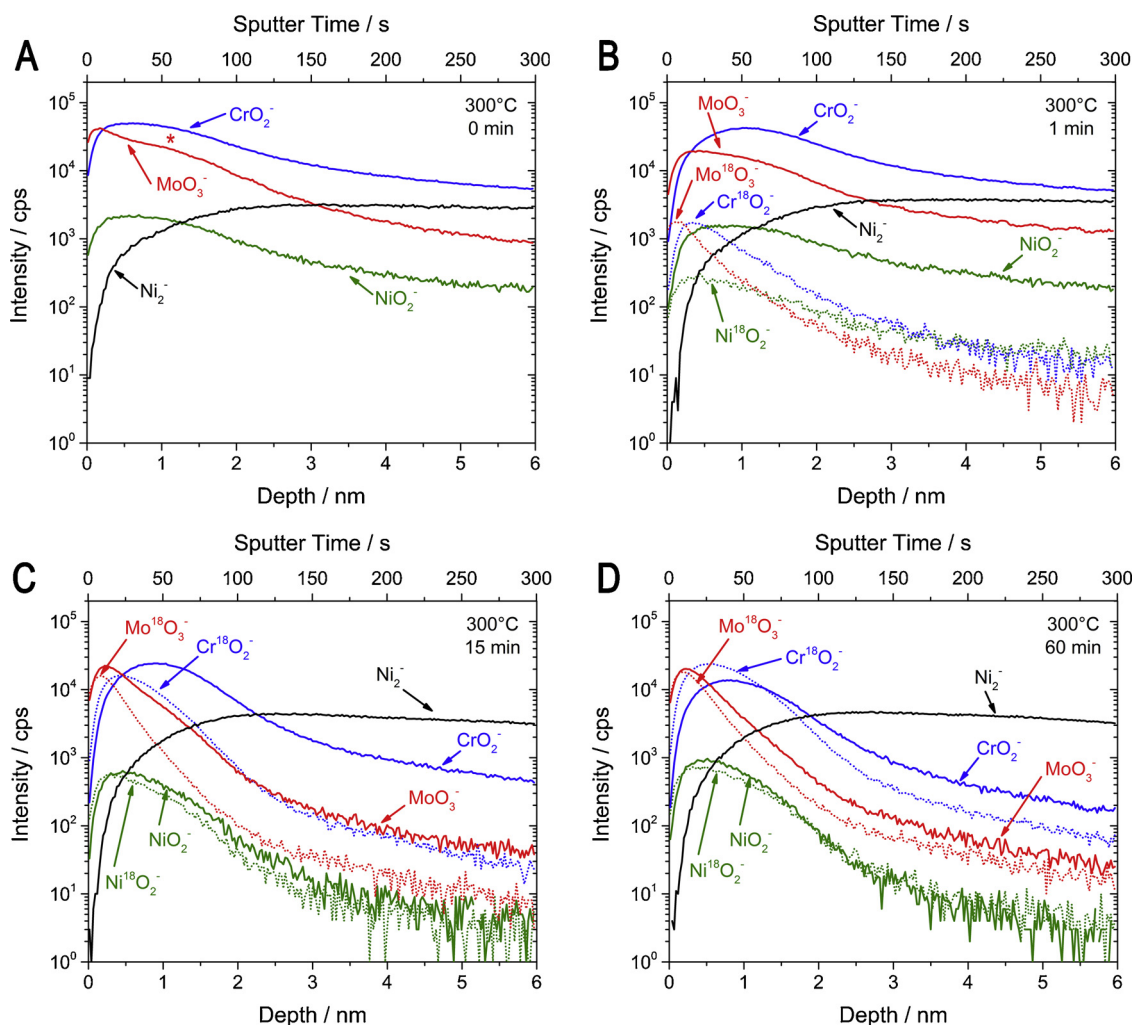
Fig. 4. ToF SIMS depth profiles of (A) the initial oxide after heating to 300 °C and of the film after (B) 1-, (C) 15-, and (D) 60-min periods of oxidation at 300 °C. The location of the unusual MoO_3^- shoulder discussed in the text is indicated by an asterisk (*). Primary Bi^+ beam operated at 1.2 pA.

Comparison of total thickness measurements in Fig. 5B showed that up to 60 min oxidation at 300 °C resulted in no major changes in thickness, with values being relatively consistent at approximately 2 nm. Furthermore, the locations of maxima for Cr- and Mo-rich layers suggested that the thickness of enriched layers remained relatively unchanged. After 5-min oxidation at 500 °C, the total oxide thickness was found to increase by approximately 5x, reaching an approximate thickness of almost 10 nm. The observed increase in thickness was a result of the growth of the inner Cr-rich oxide layer, which accounted for nearly 95% of the total film thickness at 500 °C. Interestingly, the Mo-rich layer was not found to change in thickness and continued to dominate the outermost part of the oxide film (~0.5 nm).

3.3. Mechanistic interpretation

The mechanism of oxidation was studied by following the location of ^{18}O incorporation into the oxide as a function of oxidation time. By monitoring the maximum intensity of ions that incorporated the isotopic labels (^{18}O atoms), the location of $^{18}O^{2-}$ incorporation into the oxide was inferred. Only signals from species that included the maximum number of ^{18}O atoms were considered. The signals corresponding to $Ni^{18}O_2^-$, $Cr^{18}O_2^-$, and $Mo^{18}O_3^-$, are labelled in Fig. 4B–D and Fig. 5A.

After a total oxidation time of only 1 min at 300 °C, Fig. 4B, the incorporation of ^{18}O into the oxide was rather pronounced. The local maximum signal for $Mo^{18}O_3^-$ originated from the outermost region of

the Mo-rich layer, while the $Cr^{18}O_2^-$ signal came from the outer portion of the Cr-rich barrier layer. The original MoO_3^- signal, containing ^{16}O, had a maximum intensity occurring at ~15 s sputtering time (~0.3 nm), while the maximum intensity of the $Mo^{18}O_3^-$ signal occurred at ~6 s sputtering time (~0.1 nm). Conversely, the maximum intensity of the $Cr^{18}O_2^-$ and CrO_2^- signals occurred at ~16 s sputtering time (~0.3 nm) and ~48 s sputtering time (~1 nm), respectively. The locations at which maxima occurred for $Mo^{18}O_3^-$ and $Cr^{18}O_2^-$ signals, relative to the corresponding signals for ions lacking an isotopic label, suggested the location of incorporation at the outermost interface of the respective oxide layers. Interestingly, the Mo-rich oxide appears to represent a barrier for the continued diffusion of Cr toward the outermost surface, *i.e.*, the air/oxide interface, under the experimental conditions employed herein.

With continued exposure of the specimen to $^{18}O_2$, the intensity of ^{18}O-containing signals was found to increase. After a 15 min oxidation period, Fig. 4C, the intensity of signals from ^{18}O-containing ions increased to values approximately equal to those from the analogous ^{16}O-containing ions from the initially air-formed oxide. The location of maximum intensity of the signal from ^{18}O-containing ions was again found at the outer portion of the respective Mo/Cr layers. However, beginning after 15 min of heating, isotopic exchange processes resulted in the broadening of the signals from ^{18}O-containing ions. This was attributed to the solid-state exchange of ^{18}O with ^{16}O in the oxide [19], ultimately leading to peak broadening. After an oxidation period of 60-min, Fig. 4D, the signals from ^{18}O-containing ions resembled those from
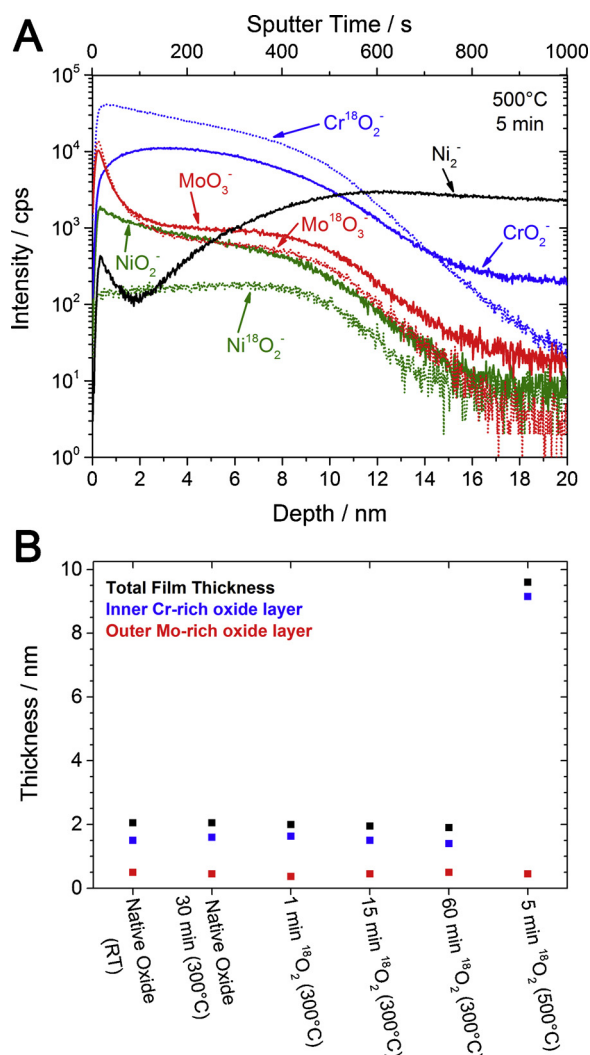
Fig. 5. (A) ToF SIMS depth profiles of the oxide after 5-min oxidation at 500 °C and (B) a summary of film thickness interpreted by ToF-SIMS depth profiles.

Fig. 6. Graphical representation of the processes occurring during the growth/maintenance of an air formed oxide at 300/500 °C.

ions containing ^{16}O in both intensity and distribution in the depth profile.

At 300 °C, the relatively constant film thickness suggested the general stability and protectiveness of the oxide film. While stable, the tendency of the oxide to incorporate ^{18}O atoms into its structure may be explained by two processes. Firstly, and most obvious, are isotopic exchange processes occurring at the outer interfaces of the respective oxide layers by the interaction of $^{18}O_2$ gas with ^{16}O atoms in the pre-existing oxide film. A second explanation involves growth processes, expected to be minor, which may have been counterbalanced by the volatilization of oxide species.

At 500 °C, increases in oxide thickness were found to be due to the growth of the inner Cr-rich layer. The location of incorporation/growth was determined to be, again, at the outer interfaces of both the CrO_2^- and MoO_3^- layers. For the thickened Cr-rich layer this was apparent due the sharp increase in intensity of $Cr^{18}O_2^-$ relative to CrO_2^-, as shown in Fig. 5B. For these growth/exchange processes to occur in the Cr-rich layer, $^{18}O^{2-}$ must have been mobile through the Mo-rich outer oxide film toward the inner Cr-rich layer. As the Mo-rich layer persisted at a relatively consistent thickness, diffusion of Mo through the Cr-rich layer was believed to have been limited.

A graphical summary that incorporates all the observations, based on the incorporation of ^{18}O, is presented in Fig. 6. The evidence suggests that both the Mo- and Cr-rich layers incorporate ^{18}O atoms at their outer interfaces, respectively. While incorporation of ^{18}O atoms occurred at the outer interface of the Mo-rich layer, the transport of O^{2-} through the Mo-rich layer must have occurred to allow the incorporation at the outer interface of the Cr-rich layer. Whether this transport process occurred *via* vacancies or interstitial sites is unclear at present. At 300 °C the incorporation of ^{18}O into the oxide is believed to be mainly the result of isotopic exchange processes while growth/volatility processes cannot be ignored. At 500 °C, the increases in film thickness makes it likely that, although not explicitly demonstrated, cation transport was a major feature in this growth/maintenance processes. The mobility of cations has been previously identified as a dominant feature of oxide growth for similar alloys [20]. Under the experimental conditions employed, the transport of Cr through the oxide appeared to be much faster than that of Mo. Following the incorporation of ^{18}O into the oxide, isotopic exchange processes spread isotope tracers throughout the oxide.

4. Conclusions

The air-formed oxide present on Hastelloy BC-1 was characterized by ToF-SIMS and XPS. The oxide was found to be composed of a bilayer structure made up of Mo- and Cr-rich regions located in the outer and inner oxides, respectively. Increased temperatures were found to cause modifications to the bilayer structure, while exposure to O_2 was found to reverse these changes. At 300 °C, the oxide thickness was unchanged relative to that of the native oxide (~2 nm), while at 500 °C, the total film thickness was found to increase to ~10 nm. This increase in thickness was due to the growth of the inner Cr-rich layer, while the thickness of the outer Mo-rich layer was unchanged relative to its thickness in the native oxide.

Insight into the transport mechanisms proceeding during gas-phase oxidation of BC-1 at 300 and 500 °C was afforded by *in situ* ToF-SIMS measurements. Incorporation of O atoms was found to occur at the outer interfaces of the Mo- and Cr-rich oxides. This demonstrated that O atoms could be transported through the outer Mo-rich layer and reach the inner Cr-rich layer. However, the Mo-rich layer appeared to prevent

or decrease the continued transport of Cr to the outermost interface.

Acknowledgments

References

[1] A. Mishra, D.W. Shoesmith, P. Manning, Materials selection for use in concentrated hydrochloric acid, Corrosion 73 (2017) 68–76.

[2] K. Hashimoto, K. Asami, A. Kawashima, H. Habazaki, E. Akiyama, The role of corrosion-resistant alloying elements in passivity, Corros. Sci. 49 (2007) 42–52.

[3] V. Maurice, P. Marcus, Current developments of nanoscale insight into corrosion protection by passive oxide film, Curr. Opin. Solid State Mater. Sci. 22 (2018) 156–167.

[4] V. Maurice, P. Marcus, Progress in corrosion science at atomic and nanometric scales, Prog. Mater. Sci. 95 (2018) 132–171.

[5] P. Marcus, Corrosion Mechanisms in Theory and Practice, CRC Press, 2011.

[6] X. Shan, J.H. Payer, Characterization of the corrosion products of crevice corroded alloy 22, J. Electochem. Soc. 156 (2009) C313–C321.

[7] J.D. Henderson, N. Ebrahimi, V. Dehnavi, M. Guo, D.W. Shoesmith, J.J. Noël, The role of internal cathodic support during the crevice corrosion of Ni-Cr-Mo alloys, Electrochim. Acta 283 (2018) 1600–1608.

[8] X. Zhang, D.W. Shoesmith, Influence of temperature on passive film properties on Ni–Cr–Mo Alloy C-2000, Corros. Sci. 76 (2013) 424–431.

[9] X. Zhang, D. Zagidulin, D.W. Shoesmith, Characterization of film properties on the Ni Cr Mo alloy C-2000, Electrochim. Acta 89 (2013) 814–822.

[10] C.-O.A. Olsson, D. Landolt, Passive films on stainless steels - chemistry, structure and growth, Electrochim. Acta 48 (2003) 1093–1104.

[11] N. Dong, C. Zhang, H. Li, B. Zhang, P. Han, A combined experimental and first-principle study on the oxidation mechanism of super austenitic stainless steel S32654 at 900 °C, Sci. Rep. 7 (2018) 1–10.

[12] H. Li, B. Zhang, Z. Jiang, S. Zhang, H. Feng, P. Han, N. Dong, W. Zhang, G. Li, G. Fan, Q. Lin, A new insight into high-temperature oxidation mechanism of super-austenitic stainless steel S32654 in air, J. Alloys Compd. 686 (2016) 326–338.

[13] V. Maurice, H. Peng, L.H. Klein, A. Seyeux, S. Zanna, P. Marcus, Effects of molybdenum on the composition and nanoscale morphology of passivated austenitic stainless steel surfaces, Faraday Discuss. 180 (2015) 151–170.

[14] M.W. Edwards, N.S. McIntyre, Gas phase initial oxidation of Incoloy 800 surfaces, Oxid. Met. 79 (2013) 179–200.

[15] X. Wu, S. Voyshnis, A. Seyeux, Y. Chumlyakov, P. Marcus, ToF-SIMS study of oxide films thermally grown on nickel-base alloys, Corros. Sci. 141 (2018) 175–181.

[16] N.S. McIntyre, T.C. Chan, C. Chen, Characterization of oxide structures formed on nickel-chromium alloy during low pressure oxidation at 500–600 °C, Oxid. Met. 33 (1990) 457–479.

[17] C.S. Tedmon Jr., The effect of oxide volatilization on the oxidation kinetics of Cr and Fe-Cr alloys, J. Electrochem. Soc. 113 (1966) 766–768.

[18] Uhlig's Corrosion Handbook, 3rd ed., Wiley, 2011.

[19] C. Poulain, A. Seyeux, S. Voyshnis, P. Marcus, Volatilization and transport mechanisms during Cr oxidation at 300 °C studied in situ by ToF-SIMS, Oxid. Met. 88 (2017) 423–433.

[20] X. Yu, A. Gulec, C.M. Andolina, E.J. Zeitchick, K. Gusieva, J.C. Yang, J.R. Scully, J.H. Perepezko, L.D. Marks, In situ observations of early stage oxidation of Ni-Cr and Ni-Cr-Mo alloys, Corrosion 74 (2018) 939–946.

[21] E. Gardin, S. Zanna, A. Seyeux, A. Allion-Maurer, P. Marcus, Comparative study of the surface oxide films on lean duplex and corresponding single phase stainless

[22] steels by XPS and ToF-SIMS, Corros. Sci. 143 (2018) 403–413.

[23] H. Peng, Composition chimique et nanostructure des films passifs formés sur acier inoxydable austénitique : effet du molybdène, Université Pierre et Marie Curie, Paris, France, 2014.

[23] S. Tanuma, C.J. Powell, D.R. Penn, Calculations of electron inelastic mean free path. II. Data for 27 elements over the 50–2000 eV range, Surf. Interface Anal. 17 (1991) 911–926.

[24] A. Mazenc, A. Galtayries, A. Seyeux, P. Marcus, S. Leclercq, ToF-SIMS study of the behavior of thermally oxidized films formed on nickel-based 690 alloy in high-temperature water, Surf. Interface Anal. 45 (2013) 583–586.

[25] X. Zhang, Z. Qin, D. Zagidulin, J.J. Noël, D.W. Shoesmith, Effect of oxide film properties on the kinetics of O2 reduction on alloy C-22, J. Electrochem. Soc. 164 (2017) C911–C917.

[26] C.R. Clayton, Y.C. Lu, A bipolar model of the passivity of stainless steel: the role of Mo addition, J. Electrochem. Soc. 133 (1986) 2465–2473.

[27] A. Srisrual, K. Pitaksakorn, P. Promdirek, Oxidation behaviour of Incoloy 800HT in pure oxygen, Materials Today: Proceedings vol. 5, (2018), pp. 9238–9243.

[28] A.Y. Musa, M. Behazin, J.C. Wren, Potentiostatic oxide growth kinetics on Ni-Cr and Co-Cr alloys: potential and pH dependences, Electrochim. Acta 162 (2015) 185–197.

[29] A.Y. Musa, J.C. Wren, Combined effect of gamma-radiation and pH on corrosion of Ni-Cr-Fe alloy Inconel 600, Corros. Sci. 109 (2016) 1–12.

[30] M.C. Biesinger, B.P. Payne, L.W.M. Lau, A. Gerson, R.C. Smart, X-ray photoelectron spectroscopic chemical state quantification of mixed nickel metal, oxide and hydroxide systems, Surf. Interface Anal. 41 (2009) 324–332.

[31] M.C. Biesinger, B.P. Payne, A.P. Grosvenor, L.W.M. Lau, A.R. Gerson, R.C. Smart, Resolving surface chemical states in XPS analysis of first row transition metals, oxides and hydroxides: Cr, Mn, Fe, Co and Ni, Appl. Surf. Sci. 257 (2011) 2717–2730.

[32] M.C. Biesinger, C. Brown, J.R. Mycroft, R.D. Davidson, N.S. McIntyre, X-ray photoelectron spectroscopy studies of chromium compounds, Surf. Interface Anal. 36 (2004) 1550–1563.

[33] P.A. Spevack, N.S. McIntyre, Thermal reduction of MoO3, J. Phys. Chem. 96 (1992) 9029–9035.

[34] E. De Vito, P. Marcus, XPS study of passive films formed on molybdenum-implanted austenitic stainless steels, Surf. Interface Anal. 19 (1992) 403–408.

[35] P. Marcus, I. Olefjord, Round Robin on combined electrochemical and AES/ESCA characterization of the passive films on Fe- Cr and Fe-Cr-Mo alloys, Surf. Interface Anal. 11 (1988) 569–576.

[36] A.N. Mansour, C.A. Melendres, Characterization of slightly hydrated Ni(OH)2 by XPS, Surf. Sci. Spectra 3 (1994) 247–254.

[37] A.N. Mansour, C.A. Melendres, Characterization of α-Ni(OH)2 by XPS, Surf. Sci. Spectra 3 (1994) 255–262.

[38] M. Lenglet, A. d'Huysser, J. Arsène, J. Bonnelle, C. Jorgensen, XANES, X-ray photo-electron and optical spectra of divalent nickel at the crystallographic transition in NiCr2O4 and the Ni1-xCuxCr2O4 system: correlation with the Jahn-Teller effect, J. Phys. C: Solid State Phys. 19 (1986) L363.

[39] J. Słoczyński, J. Ziółkowski, B. Grzybowska, R. Grabowski, D. Jachewicz, K. Wcisło, L. Gengembre, Oxidative dehydrogenation of propane on NixMg1 − xAl2O4 and NiCr2O4 spinels, J. Catal. 187 (1999) 410–418.

[40] P. Marcus, J.M. Grimal, The anodic dissolution and passivation of Ni-Cr-Fe alloys studied by ESCA, Corros. Sci. 33 (1992) 805–814.

[41] K. Lutton, K. Gusieva, N. Ott, N. Birbilis, J.R. Scully, Understanding multi-element alloy passivation in acidic solutions using operando methods, Electrochem. Commun. 80 (2017) 44–47.

[42] V. Maurice, W.P. Yang, P. Marcus, X-ray photoelectron spectroscopy and scanning tunneling microscopy study of passive films formed on (100) Fe—18Cr—13Ni single-crystal surfaces, J. Electochem. Soc. 145 (1998) 909–920.

[43] E.A. Gulbransen, K.F. Andrew, F.A. Brassart, Oxidation of Molybdenum 550° to 1700 °C, J. Electrochem. Soc. 110 (1963) 952–959.

[44] N. Cabrera, N.F. Mott, Theory of the oxidation of metals, Rep. Prog. Phys. 12 (1948) 163–184.

[45] F.P. Fehlner, N.F. Mott, Low-temperature oxidation, Oxid. Met. 2 (1970) 59–99.